



# Wall-model integrated computational framework for large-eddy simulations of wall-bounded flows

Cite as: Phys. Fluids **33**, 125120 (2021); <https://doi.org/10.1063/5.0073506>

Submitted: 30 September 2021 • Accepted: 25 November 2021 • Published Online: 13 December 2021

Yu Lv (吕钰),  Xinyi L. D. Huang (黄馨仪),  Xiaolei Yang (杨晓雷), et al.

## COLLECTIONS

Paper published as part of the special topic on [Centennial of the Kármán-Pohlhausen Momentum-Integral Approach](#)



[View Online](#)



[Export Citation](#)



[CrossMark](#)

## ARTICLES YOU MAY BE INTERESTED IN

[Grid-point and time-step requirements for direct numerical simulation and large-eddy simulation](#)

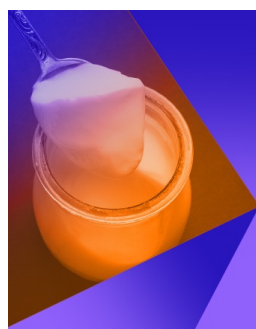
Physics of Fluids **33**, 015108 (2021); <https://doi.org/10.1063/5.0036515>

[Integral wall model for large eddy simulations of wall-bounded turbulent flows](#)

Physics of Fluids **27**, 025112 (2015); <https://doi.org/10.1063/1.4908072>

[Data-driven model for improving wall-modeled large-eddy simulation of supersonic turbulent flows with separation](#)

Physics of Fluids **33**, 126103 (2021); <https://doi.org/10.1063/5.0072550>



## Physics of Fluids

## Special Topic: Food Physics

**Submit Today!**

# Wall-model integrated computational framework for large-eddy simulations of wall-bounded flows

Cite as: Phys. Fluids **33**, 125120 (2021); doi: [10.1063/5.0073506](https://doi.org/10.1063/5.0073506)

Submitted: 30 September 2021 · Accepted: 25 November 2021 ·

Published Online: 13 December 2021



View Online



Export Citation



CrossMark

Yu Lv (吕钰),<sup>1</sup> Xinyi L. D. Huang (黄馨仪),<sup>2</sup> Xiaolei Yang (杨晓雷),<sup>1</sup> and Xiang I. A. Yang (杨翔)<sup>2,a)</sup>

## AFFILIATIONS

<sup>1</sup>State Key Laboratory of Nonlinear Mechanics, Institute of Mechanics, Chinese Academy of Sciences, Beijing 100190, China

<sup>2</sup>Department of Mechanical Engineering, Pennsylvania State University, State College, Pennsylvania 16802, USA

**Note:** This paper is part of the special topic, Centennial of the Kármán-Pohlhausen Momentum-Integral Approach.

**a)** Author to whom correspondence should be addressed: [xzy48@psu.edu](mailto:xzy48@psu.edu)

## ABSTRACT

The wall-modeled large-eddy simulation (WMLES) computational framework generally includes a wall-model solver outside the large-eddy simulation (LES) infrastructure, with the two solvers communicating only at the matching location and the wall. Having a wall-model solver outside the LES jeopardizes the performance of WMLES: first, the wall-model solver adds significant computational overhead; second, the LES solution in the wall-adjacent cell is ambiguous; and third, it is very difficult to utilize the emerging high-order numerical schemes. This paper addresses the above issues by abandoning wall-model solvers altogether and integrating wall models into LES solvers. We will employ a set of physics-inspired bases for LES solution reconstruction in the wall-adjacent cell. The methodology gives rise to a computational framework that effortlessly accounts for non-equilibrium effects in a high-order code without a stand-alone wall-model solver. We consider channel flow for a proof of concept and periodic hill for validation.

Published under an exclusive license by AIP Publishing. <https://doi.org/10.1063/5.0073506>

## I. INTRODUCTION

High Reynolds number flow problems that could only be handled by non-scale-resolving tools like Reynolds averaged Navier Stokes (RANS) before can now be handled using scale-resolving tools like large-eddy simulation (LES). A notable example is LES of an entire air-plane at flight/close-to-flight Reynolds numbers close/past stall,<sup>1,2</sup> and other examples can be found in Refs. 3–6, to name a few. In addition to the increased computational power, high Reynolds numbers LES is also enabled by wall models,<sup>7,8</sup> and the reader is directed to Refs. 9–11 for recent work on LES wall modeling. A wall-model models the flow in the wall layer, allowing a wall-modeled LES (WMLES) to resolve the  $\delta$ -scaled eddies only,<sup>12</sup> where  $\delta$  is the boundary-layer height. Figure 1 is a schematic of a wall-modeled LES (WMLES). The LES solves the (filtered) NS equation on the LES grid. Meanwhile, the wall model (WM) solves the NS equation—usually the Reynolds averaged thin boundary-layer equation—outside the LES infrastructure. Consider, e.g., the equilibrium wall model, the non-equilibrium wall model, and the integral wall model: the equilibrium wall model solves the WM equations on a 1D grid;<sup>9</sup> the non-equilibrium wall model accounts for wall-parallel convection and wall-parallel pressure gradient and solves the WM equations on a 3D grid in the wall layer;<sup>13</sup> the integral wall model solves the vertically integrated NS equation

algebraically but also outside the LES solver.<sup>14</sup> The wall model solves the flow in the wall layer, but aside from the wall flux, a wall model's solution is not part of an LES's solution. (This is, of course, not true for hybrid RANS/LES.) While many models conform to this practice,<sup>15–21</sup> having a WM solver outside the LES infrastructure is the root of many issues in WMLESs.

In the following, we explain these issues. First, not utilizing the LES infrastructure, accounting for non-equilibrium effects is difficult and computationally costly. For example, the non-equilibrium wall model relies on solvers that add a  $\sim 100\%$  computational overhead,<sup>13,22</sup> and the integral wall model solves a set of nonlinear algebraic equations whose derivation is long.<sup>14</sup> Furthermore, because wall models are developed outside the LES infrastructure, high-order LES discretizations may or may not be compatible with the WM. Among the limited work on WMLES in high-order codes, Frere *et al.*<sup>23</sup> implemented the model in Ref. 9 in a discontinuous Galerkin code and found unphysical oscillations in the wall-adjacent cells, and Lv *et al.*<sup>24</sup> had to alter their LES solver in the wall cells. Last, because the WM solution of the flow in the wall layer is not part of the LES solution, the LES solution in the wall-adjacent cell is left “unknown.” We briefly explain this issue. Consider, e.g., a second-order finite-volume code. Let us say, that we adopt the  $n$ th grid wall-model implementation in

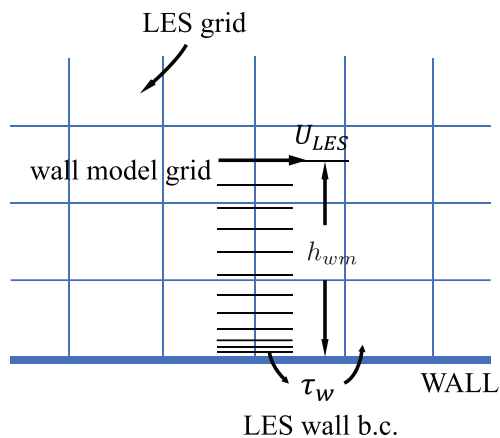


**FIG. 1.** Schematic of WMLES. The LES grid is coarse and resolves only large-scale eddies. The small-scale eddies in the wall layer are modeled. Consider, e.g., the equilibrium wall model.<sup>9</sup> It solves the WM equations (not shown here) on a 1D wall model grid. The resulting wall-shear stress is supplied to the LES as the wall boundary condition.

Ref. 9. The LES solution in the second to the  $n$ th grid follows a piecewise linear reconstruction per the finite-volume scheme, but the linear basis function cannot be applied in the wall-adjacent cell, nor could the wall-model solution. This is illustrated in Fig. 2. If one were to apply the linear basis function for solution reconstruction in the wall-adjacent cell like in Fig. 2(b), the solution gives rise to a wall velocity  $U_w = U_{h_{wm}} - \tau_w h_{wm} / (\rho \nu)$  that is negative and unphysical. Here,  $U_w$  is the wall velocity,  $h_{wm}$  is the LES/WM matching location,  $\rho$  is the fluid density,  $\nu$  is the kinematic viscosity, and  $\tau_w$  is the wall-shear

stress. Forcing the solution to give WM's gradient at the wall is also why Frere *et al.*<sup>23</sup> found oscillation in the solution. Now, if one were to take the solution of the wall model like in Fig. 2(c), the WM solution matches the LES solution at the matching location, i.e., the  $n$ th LES grid point, but not at the first off-wall LES grid points. Consequently, the LES solution contains discontinuities at the first off-wall grid, as indicated in Fig. 2(c).

This paper aims to address the above issues. We will establish a wall-model integrated computational framework for LES. We shall abandon WM solvers altogether and integrate the wall model seamlessly into the LES infrastructure. The wall model will account for non-equilibrium effects at no additional computational cost (as required by the non-equilibrium wall model) nor extra coding efforts (as required by the integral wall model).

We organize the rest of the paper as follows. The basic idea is explained in Sec. II with detailed formulation in Sec. III. We show WMLES results in Sec. IV. The paper finishes with conclusions in Sec. V.

## II. METHODOLOGY

### A. Basic idea

In this section, we explain how/why we can integrate wall-model solvers into LESs. We begin by considering a second-order finite-volume method. The solution in, e.g., wall-adjacent cell is

$$u_{//}(y) = a_1 y + a_0, \quad (1)$$

where  $u_{//}$  is the wall-parallel velocity,  $y$  is the wall-normal coordinate, and  $a_0$  and  $a_1$  are coefficients. The LES solver solves the NS equation for  $a_0$  and  $a_1$ . For brevity, we limit the discussion here in the wall-normal direction and the wall-parallel velocity component. If the resolution is such that the viscous sublayer is resolved, the velocity follows a linear scaling as a function of  $y$  in the wall-adjacent cell, and

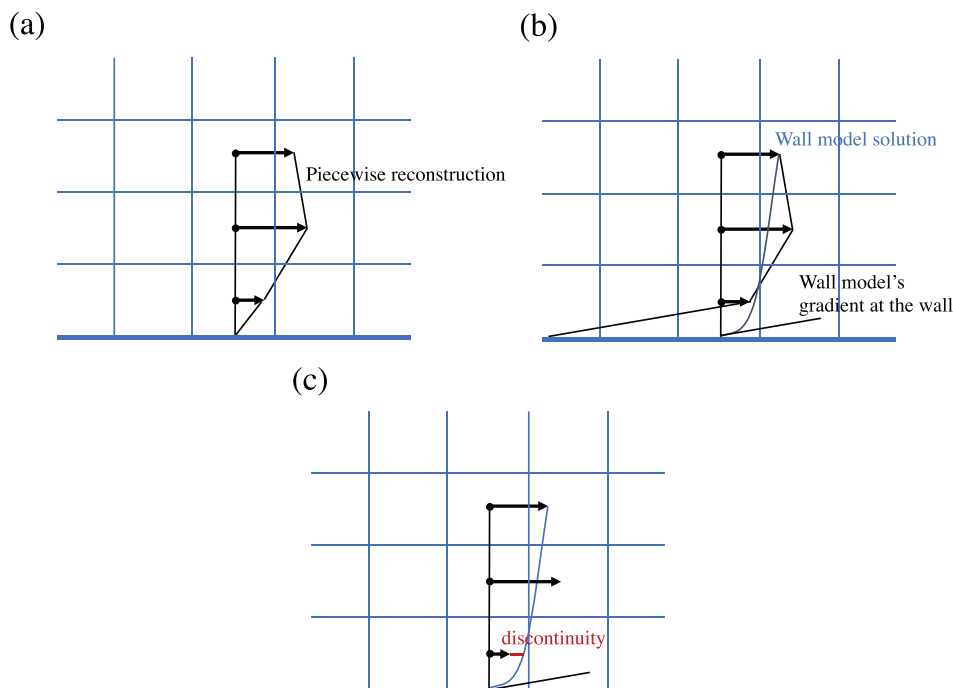


**FIG. 2.** Reconstruction of the solution in the wall-adjacent cell. (a) The LES solution if one were to impose a no-slip condition at the wall. (b) The LES solution if one were to reconstruct the solution in the wall cell by forcing the wall model's gradient at the wall. (c) The LES solution if one were to take WM's solution.

therefore the reconstruction in Eq. (1) is a close approximation of the reality. The corresponding wall-shear stress is

$$\tau_w/\rho = \nu \frac{\partial u_{//}}{\partial y} \bigg|_{y=0} = \nu a_1, \quad (2)$$

where the  $a_0$  term does not carry any wall-shear stress. If the wall layer is not resolved, the reconstruction in Eq. (1) is a poor approximation of the flow in the wall-adjacent cell, and Eq. (2) underestimates the wall-shear stress. In this case, a wall model is needed. A wall model is usually built up on the law of the wall. For low-speed flows, the logarithmic law of the wall may be written as

$$u_{//} = a_w \phi_w, \quad \phi_w(y) = \frac{1}{\kappa} \log \left( \frac{y + y_0}{y_0} \right), \quad (3)$$

where the Von Kármán constant  $\kappa$  is 0.41, and according to the law of the wall,  $a_w$  is the friction velocity  $u_\tau$ ,  $y_0$  is viscous/roughness length scale, and the wall-shear stress  $\tau_w$  is

$$\tau_w/\rho = u_\tau^2 = a_w^2. \quad (4)$$

In other words, if we view  $\phi_w$  as a basis function, the corresponding coefficient straightforwardly tells us the shear stress. In general, we may include other terms for solution reconstruction, e.g.,

$$u_{//} = a_w \phi_w + a_1 y + a_0, \quad (5)$$

where a set of bases,  $\{1, y, \phi_w\}$ , is employed. If one follows the above analysis, the shear stress carried by Eq. (5) is

$$\tau_w/\rho = a_w^2 + \nu a_1, \quad (6)$$

which is the sum of wall-shear stresses carried by the logarithmic term and linear term in order. The discussion up to this point assumes a poorly resolved wall layer. If the wall layer is resolved, the term  $\phi_w$  degenerates to a linear term (as the flow follows a linear scaling in the viscous sublayer) and may be combined with the linear  $y$  term.

In summary, we view wall modeling as solution reconstruction according to a pre-specified set of basis functions in the wall-adjacent cell. The wall-shear stress is a direct result of the solution reconstruction. Considering that an LES solver computes these coefficients [ $a_w$ ,  $a$ , and  $a_0$  in Eq. (5)], we should no longer need a stand-alone WM solver, and by abandoning WM solvers altogether, we get rid of RANS legacies in WMLES. The above is the basic idea of WM-integrated computational framework for WMLES.

This idea is inspired by the von Kármán Pohlhausen (VKP) method.<sup>25,26</sup> The basic idea of the VKP method is to project the laminar velocity profile onto a set of polynomial bases,

$$\frac{u_{//}}{u_\infty} = \beta_1 \eta + \beta_2 \eta^2 + \beta_3 \eta^3 + \beta_4 \eta^4, \quad (7)$$

where  $u_\infty$  is the freestream velocity,  $\eta = y/\delta$  is the similarity variable,  $\delta$  is the boundary-layer thickness, and  $\beta_i$  are coefficients. Pohlhausen invoked von Kármán's vertically integrated momentum equation and solved for the coefficients in Eq. (7). Although the bases in the VKP method are different from that in Eq. (5), they are both weak solutions to the NS equations.

## B. Remarks

We remark on the methodology.

### 1. Removing RANS legacies

By abandoning the WM solver, we remove RANS legacies at the same time. However, we are not the first to try to remove RANS legacies in LES. The first attempt was by Bose and co-authors.<sup>27–29</sup> They acknowledged the inadequacies of polynomials for solution reconstruction in the wall-adjacent cell. Their idea is to invoke a slip wall that sustains a non-zero turbulent flux. The slip wall eliminates the sharp velocity gradient at the wall, making it possible for solution reconstruction via polynomials. The model, however, has numerical difficulty in some codes.

### 2. Wall modeling in high-order codes

The reader may find this work reminiscent of Refs. 23 and 24, where wall modeling in DG codes is attempted. Here, we briefly review Refs. 23 and 24, and it should be clear that the two are different from the present study. In Ref. 23, Frere *et al.* solved the polynomial coefficients in LES but computed the wall flux according to the logarithmic law of the wall. The method in Ref. 24 is to add the logarithmic function as a basis in the wall-adjacent cell, but the authors chose not to remove any polynomial basis. With the additional basis function, the coefficients cannot be solved directly in LES, and Lv *et al.* solved the coefficient in front of the logarithmic term separately outside the LES solver.

### 3. Choice of basis functions

It is possible to include more terms as basis functions for solution reconstruction than those in Eq. (5). For example, one may employ the following set of basis functions for a  $Pp$  scheme:

$$\{y^i, i = 0, 1, 2, 3, \dots, p-2; \log((y - y_0)/y_0)\}. \quad (8)$$

Here, a  $Pp$  scheme is an order  $p$  scheme. For example, a P2 scheme is a second-order scheme, and a P3 scheme is a third-order scheme. The bases are terms in the Taylor expansion of the velocity around the logarithmic law of the wall. The  $y^0$  basis corresponds to wall translation. The logarithmic term is the law of the wall. The other bases account for deviations from the law of the wall. The solution is, in principle, more accurate as one increases  $p$ , but the computational cost also increases. It is quite curious to notice that except for the logarithmic term and  $y$ , other terms do not carry wall-shear stress ( $dy^i/dy = 0$  at  $y=0$  for  $i \geq 2$ ). Hence, P3 seems to be a good compromise between cost and accuracy. In fact, the integral wall model truncates at  $p=3$ . Hence, if one employs the bases in Eq. (5) for solution reconstruction in the wall-adjacent cell, (s)he is practically applying the integral wall model—but without an algebraic solver outside the LES.

### 4. Computational cost

The cost of the equilibrium wall model and the non-equilibrium wall model was reported in Refs. 30 and 31. For a grid of size  $O(10^6 - 10^7)$ , the non-equilibrium wall model adds a 100%–150% overhead to the LES, and the ODE-based equilibrium wall model adds

a 30%–40% overhead. The non-equilibrium wall model is more costly because it solves 3D RANS equations in the wall layer. The WMLESs are found to scale up to 256 cores (Intel Xeon E5–2670 2.6 GHz) for a grid of size  $10^7$ , i.e., 40 thousand points per core. The cost of the integral wall model and the algebraic equilibrium wall model is reported in Ref. 14. The cost of these two models is usually not more than 5% of the stand-alone LES. A conventional wall model incurs a computational overhead because it requires a wall-model solver outside the LES solver. We abandon wall-model solvers altogether and compute the wall fluxes in the LES solver. As a result, the integrated wall model has exactly 0 cost. That is, the cost of a WMLES with the integrated wall model is exactly the same as an LES without a wall model, and the scalability of the WMLES is solely determined by the LES solver.

### C. Wall-shear stress formulation

By integrating the WM solver into the LES solver, the WMLES no longer needs an externally supplied wall flux. Rather, the WMLES computes the wall flux within the LES solver—no different from computing a flux on an internal cell's surface. Following the notational convention,  $y$ -direction is the local wall-normal direction, and  $x$ - and  $z$ -directions are the local wall-parallel directions. The wall-parallel velocity components are

$$u_x = a'_w \phi_w + a'_1 y + a'_0, \quad u_z = a''_w \phi_w + a''_1 y + a''_0. \quad (9)$$

Here, we use  $'$  to denote quantities in the  $x$  direction and  $''$  to denote quantities in the  $z$  direction. By extending the derivation in Sec. II A, it is not difficult to show that the wall-shear stress takes the form of

$$\begin{aligned} \tau_{w,x}/\rho &= \sqrt{(a'_w)^2 + (a''_w)^2} a'_w + \nu a'_1, \\ \tau_{w,z}/\rho &= \sqrt{(a'_w)^2 + (a''_w)^2} a''_w + \nu a''_1. \end{aligned} \quad (10)$$

Specific to a P3 code, the polynomial components as functions of  $x$  and  $z$  must be included,

$$\begin{aligned} u_x &= (a'_w \phi_w + a'_1 y + a'_0)(b'_2 x^2 + b'_1 x + b'_0)(c'_2 z^2 + c'_1 z + c'_0), \\ u_z &= (a''_w \phi_w + a''_1 y + a''_0)(b''_2 x^2 + b''_1 x + b''_0)(c''_2 z^2 + c''_1 z + c''_0), \end{aligned} \quad (11)$$

and accordingly, the wall-shear stresses are

$$\begin{aligned} \tau_{w,x}/\rho &= \sqrt{(A'_w)^2 + (A''_w)^2} A'_w + \nu A'_1, \\ \tau_{w,z}/\rho &= \sqrt{(A'_w)^2 + (A''_w)^2} A''_w + \nu A''_1. \end{aligned} \quad (12)$$

where  $A'_w = a'_w(b'_2 x^2 + b'_1 x + b'_0)(c'_2 z^2 + c'_1 z + c'_0)$ ,  $A'_1 = a'_1(b'_2 x^2 + b'_1 x + b'_0)(c'_2 z^2 + c'_1 z + c'_0)$ ,  $A''_w = a''_w(b''_2 x^2 + b''_1 x + b''_0)(c''_2 z^2 + c''_1 z + c''_0)$ , and  $A''_1 = a''_1(b''_2 x^2 + b''_1 x + b''_0)(c''_2 z^2 + c''_1 z + c''_0)$ .

### III. LES SOLVER

We employ the Scalable mUlti-Physics Entropy-Stable (SUPES) solver.<sup>32</sup> The code uses a DG scheme and handles arbitrary elements (be it tetra or hex mesh). The solver has been extensively validated<sup>24,33</sup> and the DG algorithm is achievable  $10\times$  speed-up compared to a state-of-the-art finite-volume solver on unstructured meshes but remains more costly on structured curvilinear meshes.<sup>34</sup> To achieve higher computational efficiency, the SUPES is extended by

implementing a high-resolution finite-volume scheme—Piecewise Parabolic Method (PPM). Except for the wall-adjacent cells, which rely on the DG variational formulation, other cells in the computational domain are treated algorithmically with the finite-volume approach. In the following, we show further details of the solver.

### A. Governing equations

We solve the compressible LES equations in the conservative form,

$$\partial_t \bar{\rho} + \nabla \cdot (\bar{\rho} \tilde{u}) = 0, \quad (13a)$$

$$\partial_t (\bar{\rho} \tilde{u}) + \nabla \cdot (\bar{\rho} \tilde{u} \tilde{u}^T) + \nabla \bar{p} = \nabla \cdot (\bar{\tau} + \tau^{SGS}) + f, \quad (13b)$$

$$\begin{aligned} \partial_t (\bar{\rho} \tilde{E}) + \nabla \cdot (\tilde{u} (\bar{\rho} \tilde{E} + \bar{p})) &= -\nabla \cdot (\bar{q} + q^{SGS}) \\ &+ \nabla \cdot ((\bar{\tau} + \tau^{SGS}) \cdot \tilde{u}). \end{aligned} \quad (13c)$$

where  $\rho$  is the density,  $u$  is the velocity,  $p$  is the pressure,  $E$  is the total energy, and  $f$  is the body force. The Reynolds- and Favre-filtered quantities are denoted as  $\bar{(\cdot)}$  and  $(\cdot)$ . The filtered viscous stress tensor and heat flux are

$$\bar{\tau} = \mu \left[ \nabla \tilde{u} + (\nabla \tilde{u})^T \right] - \frac{2}{3} \mu (\nabla \cdot \tilde{u}) \mathbf{I}, \quad (14a)$$

$$\bar{q} = -\lambda \nabla \tilde{T}, \quad (14b)$$

where  $\mu$  is the dynamic viscosity, and  $\lambda$  is the thermal conductivity. The subgrid-scale (SGS) fluxes are

$$\tau^{SGS} = \mu_t \tilde{S}, \quad q^{SGS} = -\frac{\mu_t}{Pr_t} \nabla \cdot \tilde{h}, \quad (15)$$

where the eddy-viscosity  $\mu_t$  is evaluated per the Vreman model<sup>35,36</sup> and the turbulent Prandtl number is 0.9. The working fluid is an ideal gas, i.e.,

$$\bar{p} = (\gamma - 1) \bar{\rho} \left( \tilde{E} - \frac{\tilde{u} \cdot \tilde{u}}{2} \right), \quad (16)$$

where the adiabatic index is  $\gamma = 1.4$ . For brevity, we will omit  $\bar{(\cdot)}$  and  $(\cdot)$  in the following.

### B. Discontinuous Galerkin (DG) discretization scheme

We employ DG for discretization. The details of the DG formulation are shown below. We write the governing equations, i.e., Eq. (13), in the following compact form:

$$\partial_t \mathbf{q} + \nabla \cdot \mathbf{F}^c = \nabla \cdot \mathbf{F}^v + \mathbf{S}, \quad (17)$$

where  $\mathbf{q}$  represents the vector of solution variables in the conservative form;  $\mathbf{F}^c$  and  $\mathbf{F}^v$  denote the inviscid and viscous fluxes, respectively; and  $\mathbf{S}$  is the local source term (such as the body force). The nonlinear viscous flux, i.e.,  $\mathbf{F}^v$ , involves second-order derivatives, which is computed according to

$$\mathbf{F}^v = \mathbf{D} : \nabla \mathbf{q}, \quad (18)$$

where  $\mathbf{D}$  is the Jacobian of the diffusion flux functions with respect to the gradients of solution variables. The reader is directed to Ref. 32 for additional details of  $\mathbf{D}$ . With Eq. (18), the semi-discretized form of Eq. (17) is



$$\begin{aligned}
0 &= \int_{\Omega_e} \phi_e^T (\partial_t \mathbf{q} + \nabla \cdot \mathbf{F}^c - \nabla \cdot \mathbf{F}^v - \mathbf{S}) dx \\
&\approx \left( \int_{\Omega_e} \phi_e^T \phi_e dx \right) d_t \tilde{\mathbf{q}}_e - \int_{\Omega_e} \nabla \phi_e^T \cdot \mathbf{F}^c dx \\
&+ \int_{\partial\Omega_e} \phi_e^{T+} \hat{\mathbf{F}}^c(\mathbf{q}_e^+, \mathbf{q}_e^-, \vec{n}) ds + \int_{\Omega_e} \nabla \phi_e^T \cdot (D : \nabla \mathbf{q}_e) dx \\
&+ \int_{\partial\Omega_e} \nabla \phi_e^{T+} \cdot [D : (\hat{\mathbf{q}}_e - \mathbf{q}_e^+) \vec{n}] ds - \int_{\partial\Omega_e} \phi_e^{T+} \hat{\mathbf{F}}^v \cdot \vec{n} ds - \int_{\Omega_e} \mathbf{S} dx,
\end{aligned} \quad (19)$$

where the terms on right hand side, listed in sequence, are the temporal derivatives of solution variable, interior contribution of the convective flux, the Riemann flux, interior contribution of the viscous flux, the dual consistency term, the viscous flux term, and the local source term.  $\vec{n}$  is the outward pointing normal vector with respect to the local element  $\Omega_e$ . The Riemann flux,  $\hat{\mathbf{F}}^c$ , is specified with a local Lax–Friedrichs formulation on interior elemental interfaces, while reverts to a Euler flux with prescribed boundary state  $U^b$  on walls. The strongly imposed boundary condition, although might not converge as fast as the conventional weak boundary condition as pointed out by Collis,<sup>37</sup> rigorously enforces the conservation laws and avoids drifting of total mass/energy in the simulations of internal flows. At the interior elemental interfaces, the traces of the viscous terms are defined according to the symmetric interior penalty method,<sup>38</sup>

$$\hat{\mathbf{q}} = \{\mathbf{q}\}, \quad \hat{\mathbf{F}}^v = \{D : \nabla \mathbf{q}\} + \sigma \frac{\mu}{h} [\mathbf{q}], \quad (20)$$

in which the operators  $\{\cdot\}$  and  $[\cdot]$  are defined as  $\{\cdot\} \equiv \frac{1}{2}[(\cdot)^+ + (\cdot)^-]$  and  $[\cdot] \equiv (\cdot)^+ \vec{n} - (\cdot)^- \vec{n}$  (+ and – indicate the interior and exterior faces, respectively, with respect to the local element  $\Omega_e$ ).  $h$  denotes the size of the local elements and  $\sigma$  is a stability parameter.<sup>39</sup> On the domain boundary, the trace of the solution variable is set to a prescribed boundary state,  $U^b$ . Only the isothermal no-slip wall boundary condition is considered in this study, and  $U^b$  is set with zero velocity and a fixed temperature value. The trace of viscous momentum flux is prescribed based on the wall-shear stress, formulated in Sec. II C.

The resulting ODE system of Eq. (19) is advanced explicitly in time via a third-order Runge–Kutta scheme.

#### IV. WMLES

##### A. Cases

We consider two flows, i.e., channel flow and periodic hill. Figure 3 is a sketch of the two flows. The size of the plane channel is  $L_x \times L_y \times L_z \in 2\pi h \times 2h \times 2\pi h$ , where  $L_{x,y,z}$  is the dimension of the computational domain in the  $x$ -,  $y$ -, or  $z$ -directions and  $h$  is the half channel height. Grids of size  $N = n_x \times n_y \times n_z = 32^3$ ,  $64^3$ , and  $128^3$  are used. The grid spacing is uniform in all three directions, and there is no near-wall grid refinement. We vary the Reynolds number from  $Re_\tau = 180$ , to 2000, and 50 000, where  $Re_\tau = hu_\tau/\nu$  is the friction Reynolds number,  $\nu$  is the kinematic viscosity, and  $u_\tau$  is the friction velocity. Channel flow is very well studied. DNS data at  $Re_\tau = 180$ , and 2, 000 is publicly available.<sup>40,41</sup> The size of the periodic hill is  $L_x \times L_y \times L_z = 9H \times 3.036H \times 4.5H$  and  $L_1 = 1.929H$  (see Fig. 3 for the definition of  $L_1$ ), where  $H$  is the hill height. The hill geometry is given analytically in Appendix A of Ref. 42 and is not repeated here for brevity. Two grids are used, namely  $N = n_x \times n_y \times n_z = 64 \times 32 \times 32$ , and  $64 \times 64 \times 64$ . The grids are body fitted as sketched in Fig. 4. The flow Reynolds number is  $Re_b = HU_b/\nu = 10\,595$ , where  $U_b$  is the bulk velocity defined at the top of the hill. This periodic hill has also been extensively studied.<sup>43,44</sup> Experimental measurements and wall-resolved LES data are available in the ERCOFTAC database<sup>45</sup> and in Ref. 42, respectively. Both the channel flow and the periodic hill flow are driven by a constant body force. The boundary conditions are as follows. Periodicity is imposed in both the streamwise ( $x$ ) and the spanwise ( $z$ ) directions in the two flows. The walls are no-slip, no-penetrating, and we employ both the equilibrium wall model in Ref. 9 and the integrated wall model described in Sec. II C for wall modeling. Further details of the cases are shown in Tables I and II.

##### B. Results

In this section, we present the WMLES results. The LES solves the full NS equation, and since the solution reconstruction in the

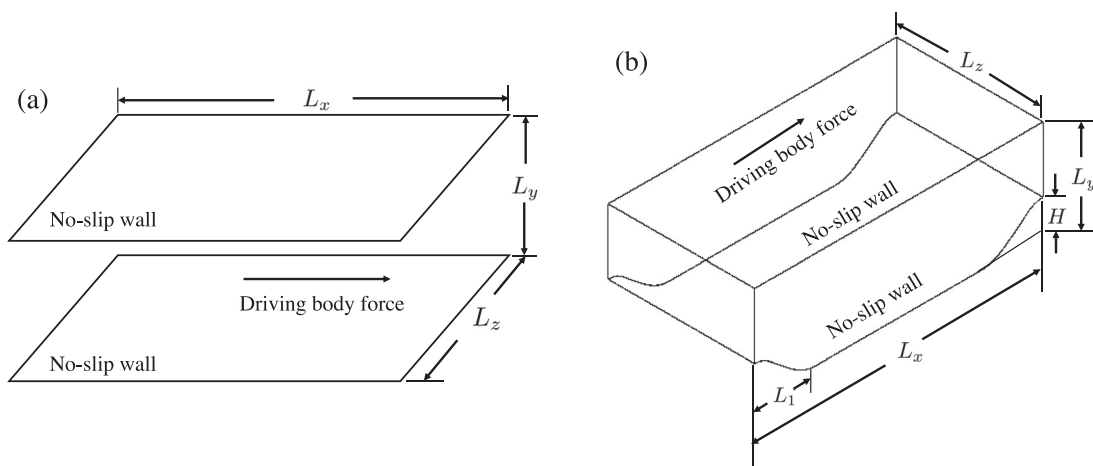
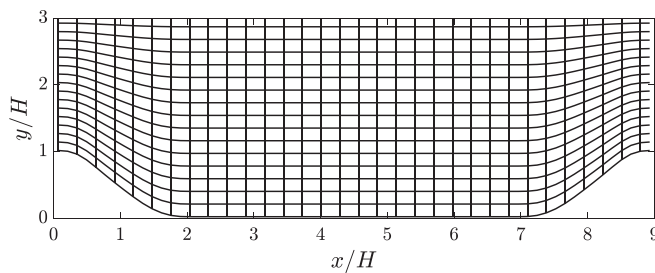


FIG. 3. (a) A sketch of the channel geometry. (b) a sketch of the periodic hill geometry.



**FIG. 4.** A sketch of the grid for the periodic hill. The grid in the FIG is of size  $n_x \times n_y = 32 \times 16$  for illustration purposes.

**TABLE I.** Details of the channel flow WMLESs. The left most column is the nomenclature. The nomenclature is as follows: Chan-[Re][grid], where [grid] may be C (coarse), R (regular), and F (fine).  $\Delta_1$  is the height of the wall-adjacent grid.

	$Re_\tau$	N	WM	$\Delta_1^+$
Chan-2kC	2000	$32^3$	Integrated WM	125
Chan-2kR	2000	$64^3$	Integrated WM	63
Chan-2kF	2000	$128^3$	Integrated WM	31
Chan-0.18k	180	$64 \times 128 \times 64$	Integrated WM	2.81
Chan-50k	50 000	$64^3$	Integrated WM	$1.6 \times 10^3$

wall-adjacent cell involves a logarithmic term, a linear term, and a constant term, the code readily accounts for non-equilibrium effects like the integral wall model.

### 1. Channel flow

Channel flow is considered as a proof of concept. First, we study the effect of grid resolution at a fixed Reynolds number  $Re_\tau = 2000$  and show that our formulation responds to the non-equilibrium effects instantaneously. Figure 5 shows the mean velocity profiles and Fig. 6 shows the velocity rms' and the Reynolds shear stress. The mean flow in WMLESs follows the DNS data closely, irrespective of the grid resolution. The velocity rms and the Reynolds shear stress in WMLESs agree more closely with the DNS as grid resolution increases—similar to other WMLESs.<sup>46,47</sup> Next, we examine how the coefficients  $a_w$  and  $a_1$  respond to the instantaneous flow. Figures 7(a) and 7(b) show the contours of the instantaneous streamwise velocity  $u$  at the first off-wall grid and the coefficient in front of the logarithmic basis function, i.e.,  $a'_w$  in Chan-2kR, where, again, the superscript ' denotes the  $x$  direction, and we use '' to denotes the  $z$  direction. We see that the coefficient  $a'_w$  correlates very well with the velocity at the

**TABLE II.** Details of the periodic hill WMLESs. The left most column is the nomenclature.

	N	WM	$\Delta_1/H$
Hill-C	$64 \times 32 \times 32$	Integrated WM	0.063–0.094
Hill-R	$64^3$	Integrated WM	0.031–0.047
Hill-Equil	$64^3$	Equilibrium wall model	0.063–0.094

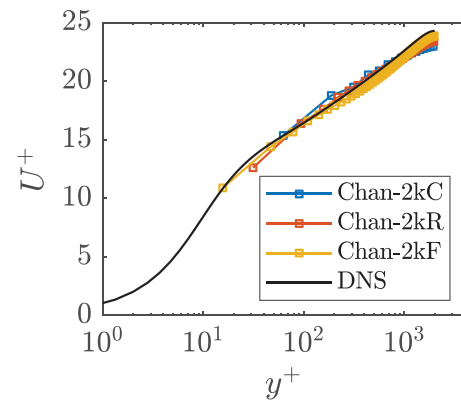


**FIG. 5.** Mean velocity profile. The symbols are WMLES with different grid resolutions, and the thin black line is the DNS.<sup>41</sup>

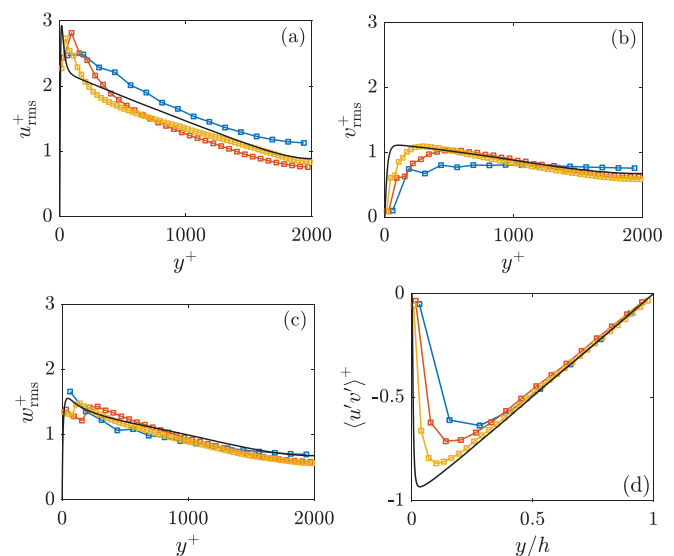


**FIG. 6.** Reynolds stresses. (a) Root mean square of the streamwise velocity fluctuation  $u_{rms}$ , (b) root mean square of the wall-normal velocity fluctuation  $v_{rms}$ , (c) root mean square of the spanwise velocity fluctuation  $w_{rms}$ , (d) Reynolds shear stress  $\langle u'v' \rangle$ . The legends are the same as in Fig. 5.

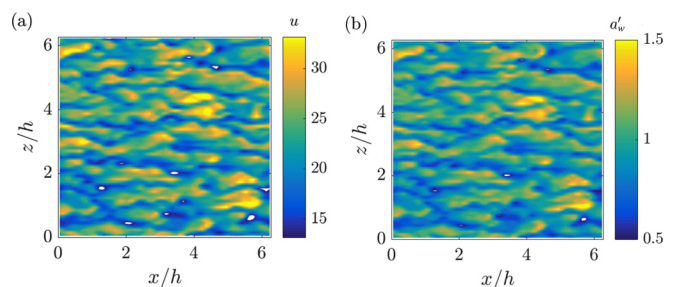


**FIG. 7.** (a) contours of the instantaneous velocity  $u$  at the first off-wall grid and (b) contours of the instantaneous coefficient  $a'_w$  in Chan-2kR. Normalization is by the wall units.

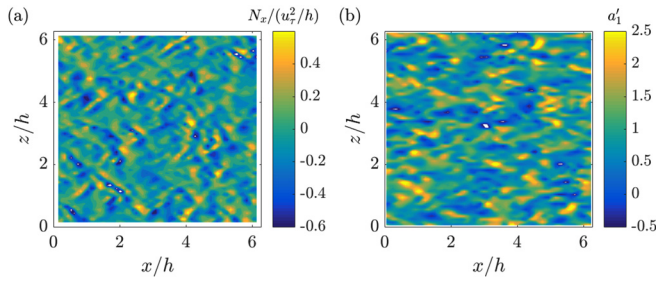


**FIG. 8.** (a) contours of the instantaneous non-equilibrium terms  $N$  at the first off-wall grid and (b) contours of the instantaneous coefficient  $a'_1$  in Chan-2kR. The coefficient  $a'_1$  is normalized by  $u_\tau^2/h$ .

first off-wall grid. This is very much expected because channel flow is an equilibrium flow, and the logarithmic mode is a good working approximation of the flow in the wall-adjacent cell.

In Sec. III, we argue that the linear term responds to and accounts for deviations from the log law like in the integral wall model. Here, we present supporting evidence. Figures 8(a) and 8(b) show contours of  $N_x$  and the coefficient in front of the linear basis function  $a'_1$ , where  $N_x = \tilde{\mathbf{u}} \cdot \nabla \tilde{\mathbf{u}} + 1/\rho \nabla p|_{y=\Delta}$  is the sum of the convective term and the pressure gradient term and measures the non-equilibrium effects at the first off-wall grid. Figures 8(a) and 8(b) have very similar patterns, but it is not immediately clear from Fig. 8 whether  $N_x$  and  $a'_1$  are correlated. Figure 9 shows the joint probability density function of  $N_x$  and  $a'_1$ , and a correlation clearly emerges. Figure 10 shows the probability density function of  $N_x$  and  $a'_1$  at the three grid resolutions, and the correlation persists across the three grids. Here, we remark on the shape of the PDFs. A coarser grid applies a more severe grid filtering. Because the flow is, on average, at equilibrium, a more severe grid filtering translates to less severe instantaneous  $N_x$  values and a more concentrated PDF of  $N_x$ . Here, we show only  $N_x$  and  $a'_1$ . The results in the spanwise direction, i.e.,  $N_z$  and  $a'_1$ , show similar trends and are not shown here for brevity.

In addition to accounting for non-equilibrium effects, the linear term would take over if the grid resolves the wall layer. Figures 11 and 12 show the mean velocity profile and the Reynolds stresses in Chan-0.18k. The WMLES grid is  $n_x \times n_y \times n_z = 64 \times 128 \times 64$  and is

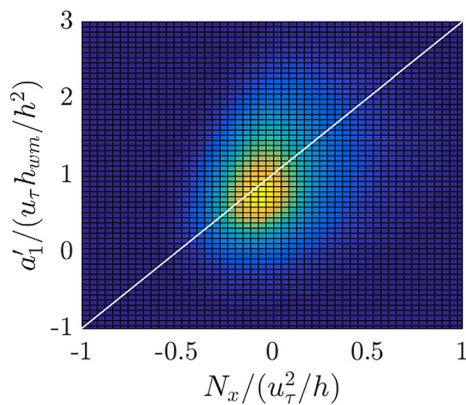


**FIG. 9.** Joint probability density function of  $N_x$  and  $a'_1$  in Chan-2kR.

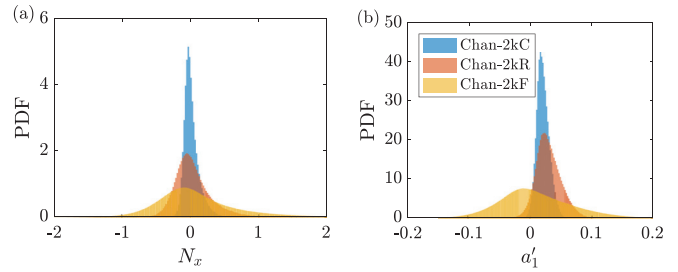


**FIG. 10.** Probability density function of (a)  $N_x$  and (b)  $a'_1$  in Chan-2kC, Chan-2kR, and Chan-2kF.

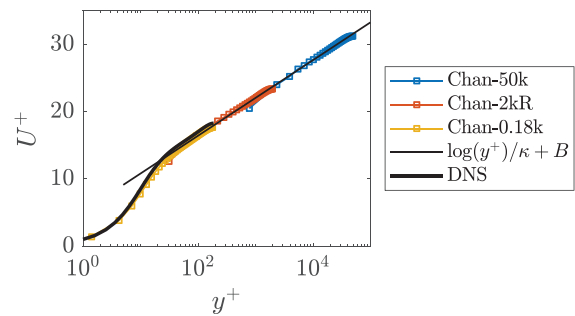


**FIG. 11.** Mean velocity profile. The symbols are WMLES with different grid resolutions, the bold black line is the DNS,<sup>40</sup> and the thin black line is the logarithmic law of the wall ( $\kappa = 0.41$ ,  $B = 5.2$ ).

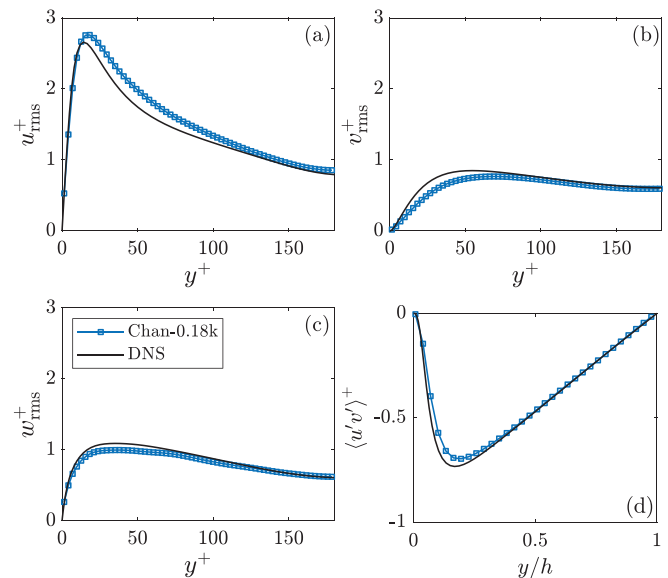


**FIG. 12.** Reynolds stresses in Chan-0.18k. The symbols are WMLES, and the lines are DNS.<sup>40</sup> (a) root mean square of the streamwise velocity fluctuation  $u_{rms}$ , (b) root mean square of the wall-normal velocity fluctuation  $v_{rms}$ , (c) root mean square of the spanwise velocity fluctuation  $w_{rms}$ , (d) Reynolds shear stress  $\langle u'v' \rangle$ .



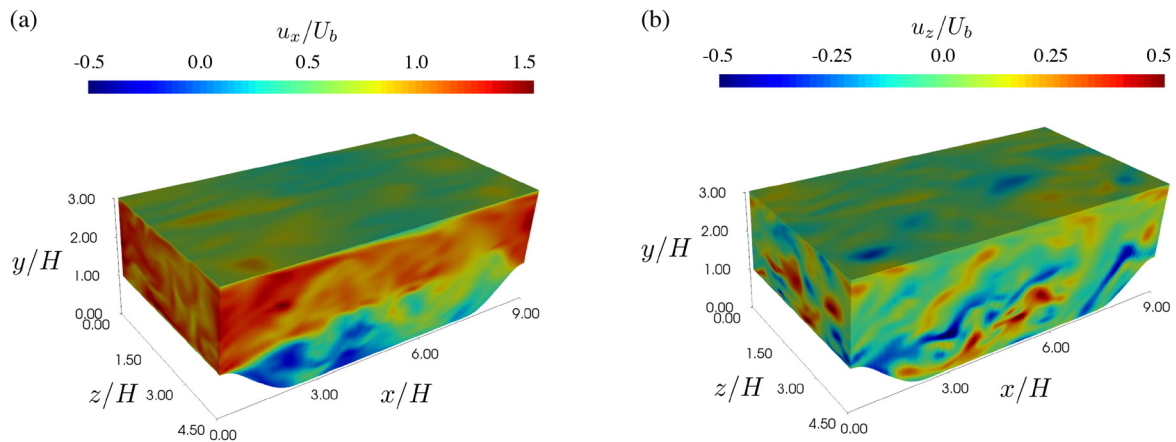


FIG. 13. Contours of (a) instantaneous streamwise velocity, and (b) instantaneous spanwise velocity in the periodic hill case, visualized by PyVT.<sup>49</sup>

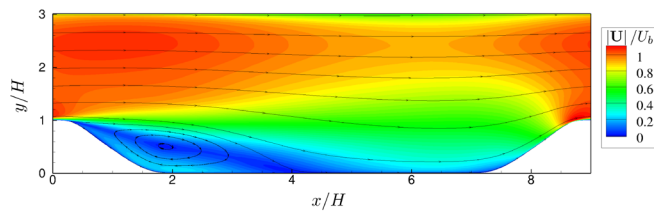


FIG. 14. Contours of the velocity magnitude and the streamlines.

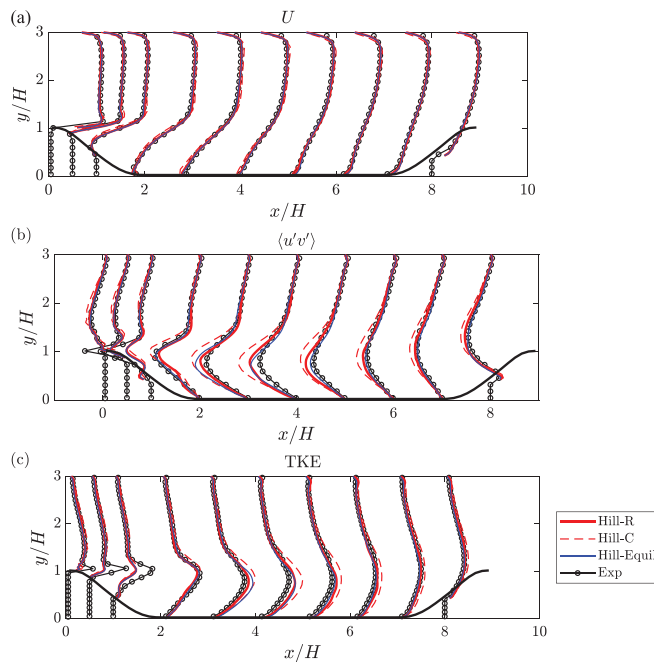


FIG. 15. (a) mean velocity, (b) Reynolds stress  $\langle u'v' \rangle$ , (c) turbulent kinetic energy profiles at various  $x$  locations. The symbols are the experiment,<sup>45</sup> the solid red lines are Hill-R, the dashed red lines are Hill-C, and the blue lines are Hill-Equil.

such that the wall is resolved. We see that the Chan-0.18k follows the DNS<sup>40</sup> closely not only in the logarithmic layer but also in the viscous sublayer and the buffer layer. The Reynolds stresses are slightly off in the buffer layer, but since the grid away from the wall is still coarse, there is no reason to expect the WMLES to match the DNS. Besides the WMLES results at  $Re_\tau = 180$ , we include the  $Re_\tau = 2000$  and 50 000 results for comparison purposes as well. We see that WMLES is able to capture the logarithmic law of the wall at any Reynolds numbers—again, without a WM solver outside the LES.

We briefly summarize. Channel flow is considered as a proof of concept. We show that the integrated wall model works fairly well for simple plane channel flow. Specifically, we show that the WMLES captures the mean flow at high and low Reynolds numbers on coarse and fine grids. We also show that by employing a P3 scheme, the linear term responds to the non-equilibrium effects like in an integral wall model.

## 2. Periodic hill

We present results for the periodic hill cases. Figure 13 shows contours of the instantaneous streamwise and spanwise velocities. We see a high speed region above  $y/H = 1$  and a low-speed region below. A shear layer emerges downstream of the hill's peak and breaks before reaching the windward side of the next hill. The flow separates at the leeside of the hill, and because of the unsteady nature of the shear layer, the separation bubble is also highly unsteady. Figure 14 shows the contours of the velocity magnitude and the streamlines of the mean flow. The flow subjects to an adverse pressure gradient and

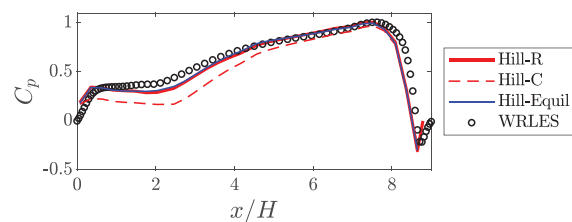


FIG. 16. Pressure coefficient. WRLES data are from Ref. 42.

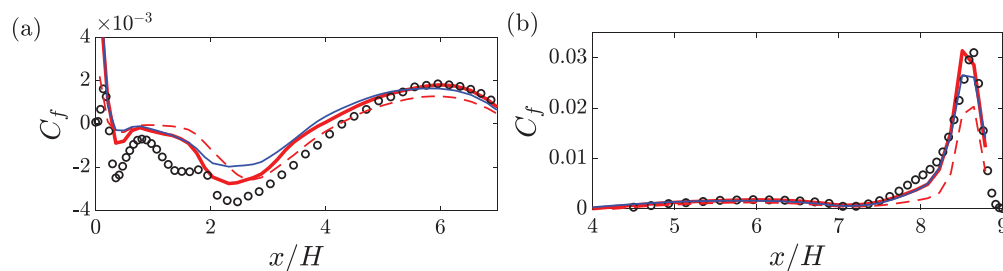


FIG. 17. Friction coefficient for the periodic hill cases. The legends are the same as in Fig. 16. (a) from  $x/H = 0$  to  $x/H = 7$ . (b) from  $x/H = 4$  to  $x/H = 9$ .

separates at the hill's leeside. The distance between the leeside and the wind side is so long that the flow reattaches before reaching the wind side.<sup>48</sup> Again, we employ a P3 scheme. The linear basis function, as we have shown in Sec. IV B 1 should be able to model the effect of pressure gradients. Hence, we expect the WM-integrated LES yield more accurate results than the equilibrium wall model. In this section, we shall see that the numerical evidence bears out our expectations.

Figure 15 shows the profiles of the mean velocity, the Reynolds stress  $\langle u'v' \rangle$ , and the turbulent kinetic energy at 10 streamwise locations. Both Hill-C and Hill-Equil capture the mean flow very well. The Reynolds stress and the turbulent kinetic energy in Hill-C and Hill-Equil are slightly off at the leeside, but the two WMLESs generally agree with the experiment. The grid seems to have a more notable impact on the results than the wall model: Hill-C, i.e., the coarse grid LES, is noticeably worse than Hill-R and Hill-Equil, i.e., the regular grid LESs. Xu *et al.* had the same observation.<sup>50</sup> They found that capturing the pressure force is more important than capturing the skin friction when pressure is the dominant momentum sink. Consequently, wall models, which concern only the friction force, are not as important as they are, e.g., in the NASA bump flow. Xu *et al.*'s finding also explain the results in Fig. 15. In fact, we see from Fig. 16 that the coarse grid WMLES Hill-C does not capture the pressure force as well as the regular grid cases Hill-R and Hill-Equil, which is why Hill-C does not do very well in capturing the mean flow.

Following the discussion above, the acid test for a wall model is the friction coefficient  $C_f = \tau_w / (2\rho U_b^2)$ . Figure 17 shows then friction coefficient. Although separation is still a difficulty and the wall models cannot capture the skin friction from 0 to about 2, we see that the Hill-R, i.e., the embedded WM, gives considerable more accurate estimates of the skin friction than Hill-Equil, i.e., the equilibrium wall model, in both the leeside and near the peak of the hill.

## V. CONCLUSIONS

We abandon WM solvers and along with it RANS legacies in LES solvers by integrating WM into LES. The method is as follows. We replace a monomial basis function with a physics-inspired basis function, in this case, the law of the wall containing both the viscous layer and the logarithmic layer. The LES solves the full NS equation including the convective term and the pressure gradient term for coefficients in front of these basis functions, and therefore we effortlessly account for non-equilibrium effects. When an LES grid is given, how well this methodology models turbulence in the wall layer depends on the LES scheme: higher-order schemes have more terms for solution reconstruction and therefore are more accurate (which, of course, is also more costly). In this work, we employ a moderate P3 scheme,

which seems to be a good compromise between cost and accuracy. The linear basis function accounts for the deviations from the logarithmic law of the wall—like the integral wall model. Again, because the LES solves the coefficient in front of the linear term, we effortlessly accounts for non-equilibrium effects in the wall layer—unlike the integral wall model and the non-equilibrium wall model, the former of which requires a long mathematical derivation and the latter of which adds  $\sim 100\%$  computational overhead. This framework is employed for plane channel and periodic hill, and the results are favorable.

This study opens up new directions for research. If one adopts the wall-model integrated computational framework for WMLES, machine learning ought to focus on finding the most appropriate basis functions (rather than finding a network that predicts the wall-shear stress<sup>42,51</sup>) Also, the wall model itself may not be the only issue in WMLES—as pointed out in Refs. 52 and 53 advances in WMLES requires novel modeling venues encompassing physical insights, together with improved gridding and numerical methods.<sup>54,55</sup> This work is along the same line: rather than working on the WM itself, we try to merge WM and LES.

## AUTHOR DECLARATIONS

### Conflict of Interest

The authors have no conflict of interest to declare.

## DATA AVAILABILITY

The data that support the findings of this study are available from the corresponding author upon reasonable request.

## REFERENCES

- <sup>1</sup>O. Lehmkuhl, G. Park, and P. Moin, "LES of flow over the NASA common research model with near-wall modeling," in *Proceedings of the Summer Program* (Center for Turbulence Research, 2016), pp. 335–341.
- <sup>2</sup>O. Lehmkuhl, G. I. Park, S. T. Bose, and P. Moin, "Large-eddy simulation of practical aeronautical flows at stall conditions," in *Proceedings of the 2018 Summer Program* (Center for Turbulence Research, 2018), pp. 87–96.
- <sup>3</sup>M. Giometto, A. Christen, P. Egli, M. Schmid, R. Tooke, N. Coops, and M. Parlange, "Effects of trees on mean wind, turbulence and momentum exchange within and above a real urban environment," *Adv. Water Resour.* **106**, 154–168 (2017).
- <sup>4</sup>Q. Li, E. Bou-Zeid, S. Grimmond, S. Zilitinkevich, and G. Katul, "Revisiting the relation between momentum and scalar roughness lengths of urban surfaces," *Q. J. R. Meteorol. Soc.* **146**(732), 3144–3164 (2020).
- <sup>5</sup>P. S. Iyer and M. R. Malik, "Wall-modeled LES of flow over a Gaussian bump," AIAA Paper No. AIAA 2020-3012, 2021.
- <sup>6</sup>M. Ge, D. F. Gayme, and C. Meneveau, "Large-eddy simulation of wind turbines immersed in the wake of a cube-shaped building," *Renewable Energy* **163**, 1063–1077 (2021).

- <sup>7</sup>H. Choi and P. Moin, "Grid-point requirements for large eddy simulation: Chapman's estimates revisited," *Phys. Fluids* **24**(1), 011702 (2012).
- <sup>8</sup>X. I. A. Yang and K. P. Griffin, "Grid-point and time-step requirements for direct numerical simulation and large-eddy simulation," *Phys. Fluids* **33**(1), 015108 (2021).
- <sup>9</sup>S. Kawai and J. Larsson, "Wall-modeling in large eddy simulation: Length scales, grid resolution, and accuracy," *Phys. Fluids* **24**(1), 015105 (2012).
- <sup>10</sup>X. I. A. Yang, G. I. Park, and P. Moin, "Log-layer mismatch and modeling of the fluctuating wall stress in wall-modeled large-eddy simulations," *Phys. Rev. Fluids* **2**(10), 104601 (2017).
- <sup>11</sup>X. I. A. Yang and Y. Lv, "A semi-locally scaled eddy viscosity formulation for LES wall models and flows at high speeds," *Theor. Comput. Fluid Dyn.* **32**(5), 617–627 (2018).
- <sup>12</sup>S. T. Bose and G. I. Park, "Wall-modeled large-eddy simulation for complex turbulent flows," *Ann. Rev. Fluid Mech.* **50**, 535–561 (2018).
- <sup>13</sup>G. I. Park and P. Moin, "An improved dynamic non-equilibrium wall-model for large eddy simulation," *Phys. Fluids* **26**(1), 37–48 (2014).
- <sup>14</sup>X. I. A. Yang, J. Sadique, R. Mittal, and C. Meneveau, "Integral wall model for large eddy simulations of wall-bounded turbulent flows," *Phys. Fluids* **27**(2), 025112 (2015).
- <sup>15</sup>M. Ma, W.-X. Huang, and C.-X. Xu, "A dynamic wall model for large eddy simulation of turbulent flow over complex/moving boundaries based on the immersed boundary method," *Phys. Fluids* **31**(11), 115101 (2019).
- <sup>16</sup>A. Wang, Y. Pan, and P. M. Markowski, "The influence of turbulence memory on idealized tornado simulations," *Mon. Weather Rev.* **148**(12), 4875–4892 (2020).
- <sup>17</sup>C. Meneveau, "A note on fitting a generalised moody diagram for wall modelled large-eddy simulations," *J. Turbul.* **21**(11), 650–673 (2020).
- <sup>18</sup>D. R. Gonzalez, M. C. Adler, and D. V. Gaitonde, "Large-eddy simulation of compressible flows with an analytic non-equilibrium wall model," AIAA Paper No. AIAA 2018-0835, 2018.
- <sup>19</sup>L. S. Freire and M. Chamecki, "Large-eddy simulation of smooth and rough channel flows using a one-dimensional stochastic wall model," *Comput. Fluids* **230**, 105135 (2021).
- <sup>20</sup>H. J. Bae and P. Koumoutsakos, "Scientific multi-agent reinforcement learning for wall-models of turbulent flows," preprint [arXiv:2106.11144](https://arxiv.org/abs/2106.11144) (2021).
- <sup>21</sup>H.-N. Wang, W.-X. Huang, and C.-X. Xu, "Synthetic near-wall small-scale turbulence and its application in wall-modeled large-eddy simulation," *Phys. Fluids* **33**(9), 095102 (2021).
- <sup>22</sup>A. Lozano-Durán, M. G. Giometto, G. I. Park, and P. Moin, "Non-equilibrium three-dimensional boundary layers at moderate Reynolds numbers," *J. Fluid Mech.* **883**, A20 (2020).
- <sup>23</sup>A. Frère, C. Carton de Wiart, K. Hillewaert, P. Chatelain, and G. Winckelmans, "Application of wall-models to discontinuous Galerkin LES," *Phys. Fluids* **29**(8), 085111 (2017).
- <sup>24</sup>Y. Lv, X. I. A. Yang, G. I. Park, and M. Ihme, "A discontinuous Galerkin method for wall-modeled large-eddy simulations," *Comput. Fluids* **222**, 104933 (2021).
- <sup>25</sup>T. Von Kármán, "Über laminare und turbulente reibung," *Z. Angew. Math. Mech.* **1**, 233–252 (1921).
- <sup>26</sup>K. Pohlhausen, "Zur näherungsweise integration der differentialgleichung der iaminaren grenzschicht," *ZAMM-J. Appl. Math. Mech./Z. Angew. Math. Mech.* **1**(4), 252–290 (1921).
- <sup>27</sup>S. T. Bose and P. Moin, "A dynamic slip boundary condition for wall-modeled large-eddy simulation," *Phys. Fluids* **26**(1), 015104 (2014).
- <sup>28</sup>X. I. A. Yang and S. T. Bose, "A physical basis of the slip-wall model for wall-modeled large-eddy simulations," in *10th International Symposium on Turbulence and Shear Flow Phenomena (TSFP10)*, Chicago (2017).
- <sup>29</sup>H. J. Bae, A. Lozano-Durán, S. T. Bose, and P. Moin, "Dynamic slip wall model for large-eddy simulation," *J. Fluid Mech.* **859**, 400–432 (2019).
- <sup>30</sup>G. I. Park and P. Moin, "Numerical aspects and implementation of a two-layer zonal wall model for les of compressible turbulent flows on unstructured meshes," *J. Comput. Phys.* **305**, 589–603 (2016).
- <sup>31</sup>G. I. Park, "Wall-modeled large-eddy simulation of a high Reynolds number separating and reattaching flow," *AIAA J.* **55**(11), 3709–3721 (2017).
- <sup>32</sup>Y. Lv, "Development of a nonconservative discontinuous Galerkin formulation for simulations of unsteady and turbulent flows," *Int. J. Numer. Methods Fluids* **92**(5), 325–346 (2020).
- <sup>33</sup>Y. Lv and M. Ihme, "Entropy-bounded discontinuous Galerkin scheme for Euler equations," *J. Comput. Phys.* **295**, 715–739 (2015).
- <sup>34</sup>Y. Lv, P. C. Ma, and M. Ihme, "On underresolved simulations of compressible turbulence using an entropy-bounded DG method: Solution stabilization, scheme optimization, and benchmark against a finite-volume solver," *Comput. Fluids* **161**, 89–106 (2018).
- <sup>35</sup>A. Vreman, "An eddy-viscosity subgrid-scale model for turbulent shear flow: Algebraic theory and applications," *Phys. Fluids* **16**(10), 3670–3681 (2004).
- <sup>36</sup>D. You and P. Moin, "A dynamic global-coefficient subgrid-scale model for compressible turbulence in complex geometries," *Annu. Res. Briefs, Cent. Turbul. Res.* **2008**, 189–196.
- <sup>37</sup>S. S. Collis, "Discontinuous Galerkin methods for turbulence simulation," in *Proceedings of the Summer Program* (Center for Turbulence Research, 2002), pp. 155–167.
- <sup>38</sup>R. Hartmann and P. Houston, "Symmetric interior penalty DG methods for the compressible Navier–Stokes equations II: Goal-oriented a posteriori error estimation," *Int. J. Numer. Methods Eng.* **3**(2), 141–162 (2006).
- <sup>39</sup>K. Shahbazi, "An explicit expression for the penalty parameter of the interior penalty method," *J. Comput. Phys.* **205**(2), 401–407 (2005).
- <sup>40</sup>J. Kim, P. Moin, and R. Moser, "Turbulence statistics in fully developed channel flow at low Reynolds number," *J. Fluid Mech.* **177**, 133–166 (1987).
- <sup>41</sup>S. Hoyas and J. Jiménez, "Scaling of the velocity fluctuations in turbulent channels up to  $Re_\tau = 2003$ ," *Phys. Fluids* **18**(1), 011702 (2006).
- <sup>42</sup>Z. Zhou, G. He, and X. Yang, "Wall model based on neural networks for LES of turbulent flows over periodic hills," *Phys. Rev. Fluids* **6**(5), 054610 (2021).
- <sup>43</sup>C. Rapp and M. Manhart, "Experimental investigations on the turbulent flow over a periodic hill geometry," in *TSFP5* (Begel House Inc., 2007).
- <sup>44</sup>W.-J. Lin, M.-J. Li, C.-W. Su, X.-Y. Huang, and C.-A. Lin, "Direct numerical simulations of turbulent periodic-hill flows with mass-conserving lattice Boltzmann method," *Phys. Fluids* **32**(11), 115122 (2020).
- <sup>45</sup>ERCOFTAC, see <http://cfd.mace.manchester.ac.uk/ercoftac/> for "Ercoftac Classic Collection Database."
- <sup>46</sup>L. Wang, R. Hu, and X. Zheng, "A comparative study on the large-scale-resolving capability of wall-modeled large-eddy simulation," *Phys. Fluids* **32**(3), 035102 (2020).
- <sup>47</sup>H. J. Bae, A. Lozano-Duran, S. Bose, and P. Moin, "Turbulence intensities in large-eddy simulation of wall-bounded flows," *Phys. Rev. Fluids* **3**(1), 014610 (2018).
- <sup>48</sup>L. Temmerman and M. A. Leschziner, "Large eddy simulation of separated flow in a streamwise periodic channel constriction," *Second Symposium on Turbulence and Shear Flow Phenomena* (Begel House Inc., 2001).
- <sup>49</sup>Q. Liu, Z. Qiao, and Y. Lv, "PyVT: A python-based open-source software for visualization and graphic analysis of fluid dynamics datasets," *Aerosp. Sci. Technol.* **117**, 106961 (2021).
- <sup>50</sup>H. H. Xu, X. I. A. Yang, and P. M. Milani, "Assessing wall-modeled large-eddy simulation for low-speed flows with heat transfer," *AIAA J.* **59**(6), 2060–2069 (2021).
- <sup>51</sup>X. I. A. Yang, S. Zafar, J.-X. Wang, and H. Xiao, "Predictive large-eddy-simulation wall modeling via physics-informed neural networks," *Phys. Rev. Fluids* **4**(3), 034602 (2019).
- <sup>52</sup>A. Lozano-Durán and H. J. Bae, "Self-critical machine-learning wall-modeled LES for external aerodynamics," preprint [arXiv:2012.10005](https://arxiv.org/abs/2012.10005) (2020).
- <sup>53</sup>A. Lozano-Durán, S. T. Bose, and P. Moin, "Performance of wall-modeled LES with boundary-layer-conforming grids for external aerodynamics," preprint [arXiv:2107.01506](https://arxiv.org/abs/2107.01506) (2021).
- <sup>54</sup>J.-E. Schumann, S. Toosi, and J. Larsson, "Assessment of grid anisotropy effects on large-eddy-simulation models with different length scales," *AIAA J.* **58**(10), 4522–4533 (2020).
- <sup>55</sup>I. Hayat and G. I. Park, "An efficient implementation of the ODE equilibrium wall model using Gauss quadrature method," in *APS Division of Fluid Dynamics* (2020).